Flow field and forces on a highly curved plate

Thomas Goulven, Patrick Bot, Benoît Habert

13th International Symposium on Particle Image Velocimetry – ISPIV 2019
Munich, Germany, July 22-24, 2019

Flow field and forces on a highly curved plate

Goulven Thomas[1*], Patrick Bot[1], Benoit Habert[1]

[1] Naval Academy Research Institute-IRENav, Brest, France

[*] goulven.thomas@ecole-navale.fr

Abstract

While both slender wings and bluff bodies are the usual focus of classical fluid dynamics, the behavior of a high-lift not-so-slender body remains somehow original. This work presents an experimental investigation of a high-camber curved thin plate with a sharp leading edge, in a wide range of angle of attack (-10° to 28°), at a Reynolds number of $1.82.10^5$. Forces are measured with a strain-gauge balance and the flow field is determined thanks to time-resolved 2D Particle Image Velocimetry (PIV) in a nominally 2D flow. Despite this very simple geometry, the section generates a high lift and shows a rather original behavior, with characteristics of both bluff and slender lifting bodies. The sectional lift coefficient is estimated by the velocity circulation around the section from the PIV fields. The time-averaged lift computed from the circulation compares reasonably well with the lift measured by the force balance, even in the presence of flow separation. Furthermore, the sectional lift coefficient time series enables a detailed spectral analysis of the flow behavior, highlighting the vortex shedding in the wake. The flow pattern is characterized with a vortex identification method, and the transition between a wing-like flow and bluff-body-like flow is evidenced. It is shown that when the angle of attack exceeds 10°, the lift is sharply increased with a reduction of trailing edge separation, as a consequence of an earlier transition of the boundary layer on the suction side, triggered by separation at the sharp leading edge.

1 Introduction

Fluid mechanics generally separates obstacles in the flow in two types. Bluff bodies defined as low lift/drag ratio profiles with a large wake and important vortex shedding. On the other side, slender bodies with a low camber and rounded leading edge characterized by a high lift/drag ratio and thin wake until the stall. Thin cambered plates have recently gained interest for applications in Micro-Air Vehicles (MAV) as they have been shown to outperform classical wing sections at low Reynolds number Sunada et al. (2002), Laitone (1996) and Hein and Chopra (2007). High-camber sections generate a high lift and a high drag contrary to typical wing sections that focus on a great lift/drag ratio. Such sections are used for landing planes or yacht downwind sails. These kinds of airfoils generate high lift but they still find an advantage having high drag depending on the situation. A simple increase of the angle of attack totally modifies the airfoil behavior. From previous studies with the same geometry, this section has shown a rather original behavior, with characteristics of both bluff and slender lifting bodies. First, a lift crisis was evidenced simultaneously to the classical drag crisis well known on cylinders Bot et al. (2016): for a fixed, low, angle of attack, the lift suddenly jumps when the Reynolds number exceeds a critical value. Moreover, when sweeping the angle of attack, two types of polar curves were found depending on the Reynolds number Lombardi (2014). At low Re, the flow generally shows strong separation. When the angle of attack exceeds a critical value around (12°15°), the flow separates at the sharp leading edge and reattaches to form a leading edge vortex, triggering the transition to turbulence, what makes the rear separation point move downstream on the suction side, resulting in a jump in lift. At high Re, separation is much more reduced for moderate angles of attack and the lift if high. When increasing, a two-stage stall is observed: after a first drop, the lift bounces back up when separation occurs at the leading edge before complete stall takes place for higher angles. Then, the transition between sub-critical regime (massively detached flow) and super-critical regime (reduced separation) can be obtained by varying the Reynolds number or the angle of attack. Detailed PIV measurements focused on the leading edge showed that the occurrence of a sustained Leading Edge Vortex is linked to an increase in lift Habert (2018).

Experiments have been carried out in the IRENav hydrodynamic tunnel to measure the forces and velocity field on a high-camber thin section with a sharp leading edge made of a cambered plate, in a nominally 2D flow. A wide range of angle of attack (from -10° to 28°) is investigated for a Reynolds number in the transitional range ($Re = 1.82.10^5$). This work presents a dynamic investigation based on time-resolved PIV and forces time series. The global lift coefficient is determined from direct force measurements with a hydrodynamic balance and the sectional lift coefficient is given by the velocity circulation on a closed contour around the section, computed from the velocity fields. The aim is to compare these values and show their similar behaviors even in high separation flow pattern. It will allow us to investigate the lift coefficient time series from velocity circulation that should be particularly useful to study the dynamic features of the flow. The evolution of the sectional lift coefficient over time is compared with the corresponding velocity fields. The evolution of the lift coefficient compares with corresponding velocity fields; different flow patterns and spectral analysis on lift coefficient signals are examined. The last part of this work is an investigation of the structure of the wake with the help of vortex identification methods developed by Graftieaux et al. (2001). Resulting observations may support the idea of a transition from sub-critical to super-critical regime.

2 Experimental methods

Experiments were carried out in the IRENav hydrodynamic tunnel, the general architecture and the test section are shown in Figure 1, to measure the forces and velocity fields on a two-dimensional high-camber plate. The test section is 1m long and 192mm x 192mm. This plate is a circular arc section machined on a 100mm diameter and 3mm thick stainless steel cylinder Figure2. The chord length is c=74.45mm, a camber ymax=16.6mm located at mid-chord, resulting in a relative camber t/c=22.3% and a span b=191.5mm that almost fill the test section width to avoid contacts and friction with the wall that could disturb force measurements.

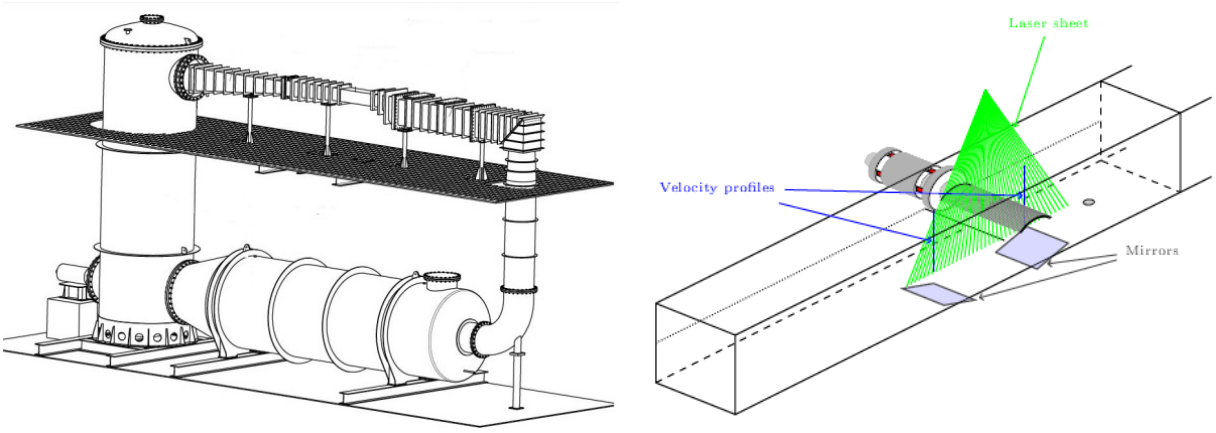

Figure 1: IRENav hydrodynamic tunnel and tunnel test section

The upstream flow velocity in the tunnel test section can be adjusted. During this campaign, the upstream velocities of 3 m/s have been tested. That corresponds to a Reynolds number in the transitional range of $1.82.10^5$. The Reynolds number for all experiments was calculated based on the chord length. The plate is connected to a hydrodynamic balance using strain gauges that allow measuring lift and drag forces. A wide range of angle of incidence (from -10° to 28°) is investigated using a rotating frame mounted on bearings and driven in rotation by a stepper motor where the balance is fixed. Balance strain gauges measure electric signals convert to forces thanks to a previous calibration. Forces are recorded for 20 seconds at 1 kHz. A description of the hydrodynamic balance can be found in Marchand (2014). It returns the global mean lift coefficient defined below (idem for drag and torque):

$$\bar{C}_{L\cdot bal} = \frac{2L}{\rho \cdot c \cdot b \cdot U_0^2} \tag{1}$$

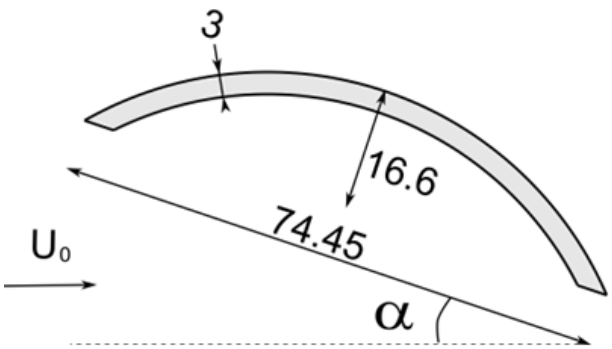

Figure 2: Highly curved plate tested, dimension in mm

These measurements are coupled with velocity field acquisition with 2D particle image velocimetry (PIV). As shown in Figure 1, a laser sheet is set from above the test section, located at mid-span using the Litron Lasers LDY303 PIV diode pump, dual cavity (from 0.2 to 20 kHz repetition rate and 20 mJ output energy at 1 kHz). This laser sheet illuminates m_sized polyamide particles seeded in the flow. Two mirrors are placed below the test section to reflect the laser sheet on the same plan and to illuminate the lower side of the plate. This set-up allows the acquisition of the entire flow around the plate. For each AoA, 1000 pairs of images are visualized with a Phantom v611 6Gpx/s camera (1280x800 pixels resolution recorded at a maximum of 6242 fps) with Dantec's DynamicStudio at a sampling frequency of 500 Hz. Images are pre-processed to subtract the background, to normalize illumination inhomogeneity and processed with the AdaptivePIV algorithm proposed by Dantec's DynamicStudio Dantec (2013). The final interrogation area is 32 x 32 pixels with a 50% overlap and typically 3 correlation passes are used. 1000 instantaneous and a mean vectors fields are obtained for each AoA. Post-processing have been done further as detachment points locations, by searching change in the sign of velocity vectors along the suction-side (upper-side) of the profile; sectional lift, obtained using the velocity circulation on a closed contour around the profile; or detection of vortices helped by a vortex detection method developed by Graftieaux et al. (2001).

2.1 Sectional lift computed by circulation

To compare the forces acquired from the hydrodynamic balance and to analyze the lift coefficient evolution in time, a sectional lift coefficient is obtained from the PIV velocity field computing the velocity circulation on a closed contour around the obstacle:

$$\Gamma = \oint V \cdot ds \tag{2}$$

From the expression to compute the lift, due to the Kutta-Joukowski theorem for a 2D potential flow I.L. Ryhming(1985), we obtained a relation between the sectional lift coefficient and the velocity circulation:

$$C_{L_\Gamma}(t) = \frac{2\Gamma}{c \cdot U_0} \tag{3}$$

Indeed, this method gives a value of the sectional lift coefficient for each instantaneous velocity field acquired from AdaptativePIV and allows observing lift variations over time. A spectral analysis is carried out using the Welch method Welch (1967).

2.2 Vortex detection criteria

High-frequency PIV acquisition enables to observe vortex shedding phenomenon contained in a range of 20 to 100 Hz. The evolution of vortex identification method allows for better comprehension of these phenomena. The 1 and 2 criteria, corresponding to vortex center identification and vortex boundary identification are Eulerian method developed by Graftieaux et al. (2001). Vortex shedding areas on the flow field are driven by high-velocity gradient with important vorticity as shear areas. The Γ_2 criterion is more relevant for vortex

identification on velocity field from PIV than vorticity, sensitive to noise. Expressions defining this criterion are defined below, Figure 3 represents the detection algorithm.

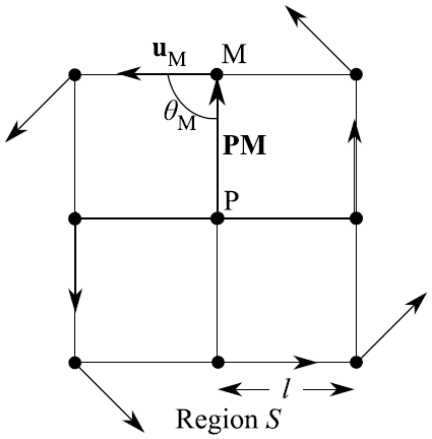

Figure 3: Vortex detection algorithm

The dimensionless scalar function Γ_2 is defined as:

$$\Gamma_2(P) = \frac{1}{N}\sum_S \frac{[PM \wedge (U_M - \tilde{U}_P)].z}{\|PM\| \cdot \|U_M - \tilde{U}_P\|} \tag{4}$$

Where S is a two-dimensional area surrounding P and z is the unit vector normal to the measurement plane. —2— is a dimensionless scalar bounded by 1. The boundary identification criterion Γ_2, is derived from the vortex center identification function and takes into account a local convection velocity.

$$\tilde{U}_P = \frac{1}{N}\sum_S U_M \tag{5}$$

The size of the domain, defined by N (the number of points in the neighborhood) is an important parameter to fix at the beginning. Indeed, the smaller the domain, the more discretized the final contour, but the noisier the 2 field. Rotating areas are defined for typical values of the Γ_2 criterion:
$|\Gamma_2| < \frac{2}{\pi} \rightarrow$ Flow dominated by convection
$|\Gamma_2| = \frac{2}{\pi} \rightarrow$ Pure shear
$|\Gamma_2| > \frac{2}{\pi} \rightarrow$ Flow dominated by rotation

3 Results and discussion

The experimental campaign and different processes give results concerning the lift and velocity fields. Presented results should allow for a better comprehension of original behaviors observed on the high-camber thin section with a sharp leading edge. First, the lift coefficient obtained from the hydrodynamic balance is compared to the sectional lift coefficient computed from the velocity circulation. A good correlation, allows us to analyze velocity fields to the sectional lift coefficient time-series evolution to show the relation between the shape of the flow and lift coefficient variations. This first investigation is supported by the evolution of the detachment point location and the spectral analysis. The last results present the vortex detection criterion method and its usefulness to analyze the flow topology around the plate comparing to velocity fields.

3.1 Lift coefficient computation

The velocity circulation on a closed contour around an obstacle presented in 2.1, permits to compute the sectional lift coefficient from velocity fields. A comparison is made between the global lift from the hydrodynamic balance and the sectional lift coefficient computed from PIV fields. For a Reynolds $Re = 1.82.10^5$,

a wide range of angle of attack is investigated (from -10° to 28°) with steps from 0.5° to 2°. Both acquisitions (Forces and PIV) are made by increasing the AoA until 28° and then on the return by decreasing the AoA on selected points of interest. A comparison of the two lift coefficient results is presented in Figure 4. As the figure shows, lift coefficients from both methods agree reasonably well. Moreover, variations and knee-points of both curves are simultaneous. The mean gap between lift coefficients from PIV and hydrodynamic balance is about 8% with a minimum gap percentage of 0.1% and a maximum of 27%. In fact, our results show that before 2° of incidence lift coefficients are truly similar to each other. After 2°, an almost constant gap takes place. This difference is certainly due to 3D effects on the flow. In fact, the velocity circulation method is applied to a 2D section of the flow at mid-span. It cannot take into account 3D effects as the hydrodynamic balance. A small hysteresis loop is evidence d when increasing or decreasing the angle of attack between 8° and 10°. Our finding demonstrates their similar behaviors even in high separation flow pattern. These observations allow an investigation of 2D section flows to compare the sectional lift coefficient time-series evolution to corresponding velocity fields.

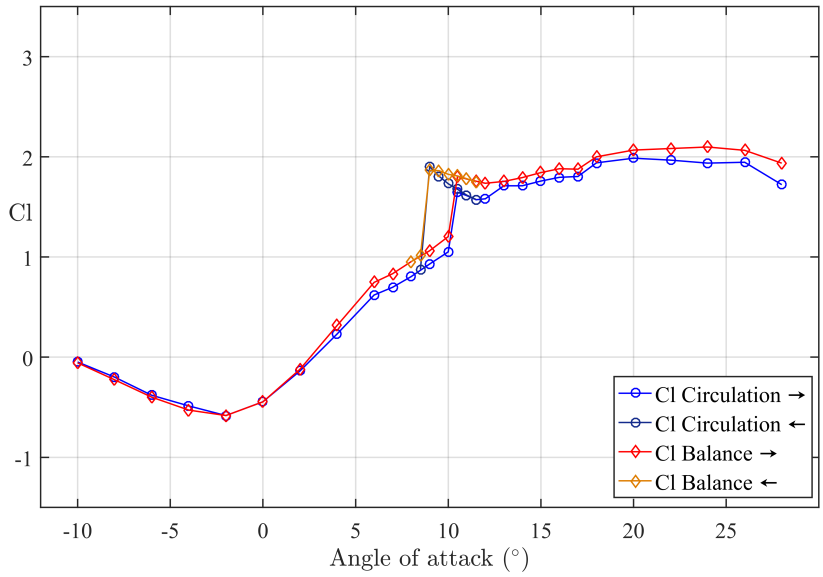

Figure 4: Lift coefficient comparison from hydrodynamic balance and circulation computation for both increasing → and decreasing ← AoA

3.2 Sectional lift coefficient and snapshot velocity fields

PIV measurements are acquired and post-processed as explained in the experimental set-up on the same results as part 3.1, for $Re = 1.82.10^5$. For each AoA, 1000 image pairs are recorded at a frequency of 500Hz giving 1000 snapshots of the instantaneous flow field and the corresponding evolution of the sectional lift coefficient over 2 seconds. In a further approach, an original behavior is developed. As observed in Figure 4, a sharp lift jump occurs at angles of attack between 10° and 10.5°. Concerning velocity circulation computation, the sectional lift coefficient jumps from 1.05 to 1.65 in the increasing part. To clarify this phenomenon, velocity fields and lift coefficient evolution of the surrounding lift jump AoA are presented in Figure 5. Great differences are observed on snapshot fields, the wake width is more consequent at 10° than 10.5° such as the typology of the wake. Indeed, the wake oscillations are more significant before the transition than after. With high separation Figure 5(a), the sectional lift shows strong oscillations related to the vortex shedding Figure 5(c). With lesser separation Figure 5(b), the mean sectional lift is higher and fluctuations reduced significantly Figure 5(d). The AoA exceeds a critical value triggering the transition to turbulence, a transition between sub-critical regime (massively detached flow) and super-critical regime (reduced separation). The following process investigating the detachment point location and the spectral analysis support the previous comparison between the sectional lift coefficient time series and the corresponding velocity field.

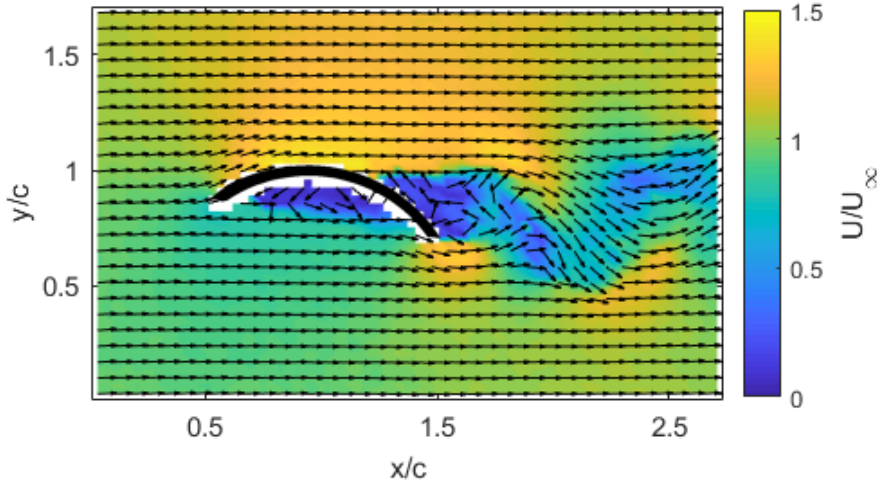

(a)

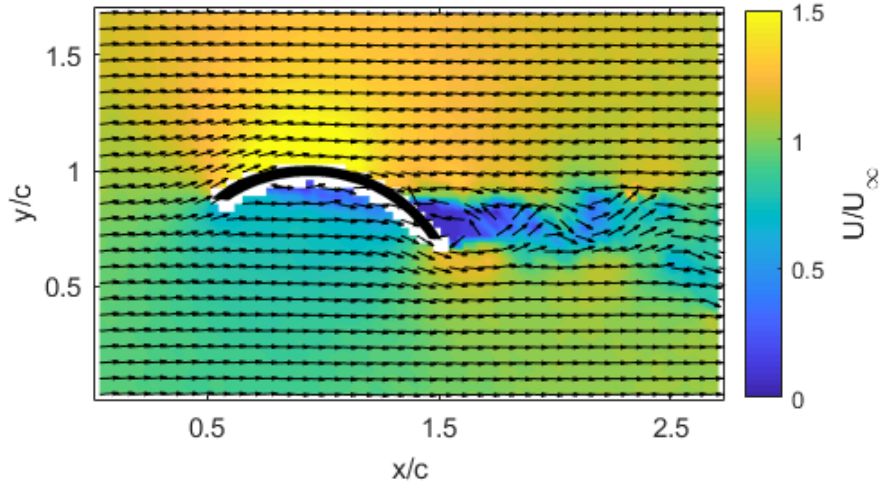

(b)

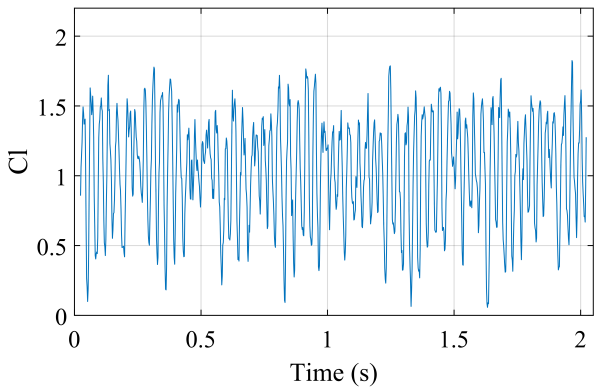

(c)

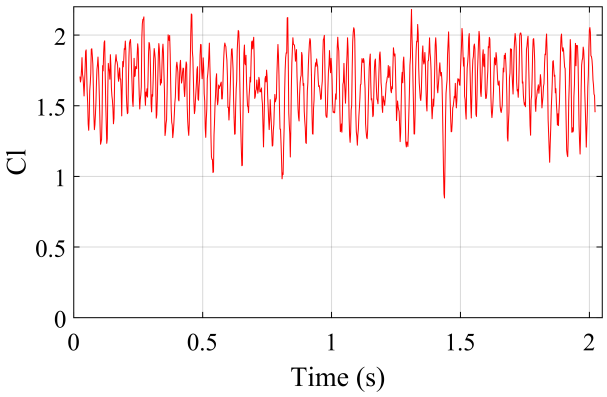

(d)

Figure 5: Snapshot velocity fields (a), (b) and Lift coefficient evolution (c), (d) at $Re = 1.82.10^5$ before the transition, for (a), (c) AoA = 10° and after (b), (d) AoA = 10.5°

3.3 Detachment point location and spectral analysis

The wake width diminution highlighted in the previous section is clearly demonstrated on the histogram representing the detachment point location depending on the AoA Figure 6(a). From -10° to 10°, the detachment point moves back along the profile plate from 0.95 to 0.65 x/c. At 10.5°, it moves forward instantly to reach 0.8 x/c position and start moving backward again. Slowly on a first time until the stall at 24° where the detachment point shrinks to the leading edge.
Spectral analysis, using the Welch method is performed on the lift coefficient time series, for each angle of attack at the same Reynolds number $Re = 1.82.10^5$. Power density spectra for each AoA are displayed in Figure 6(b), revealing significant frequency peaks between 30Hz and 40 Hz, from -10° to 10° AoA. These frequencies can be explained with the adimensional Strouhal number describing oscillating flow mechanisms. Where f is the characteristic frequency, U0 the upstream velocity and L(AoA) the characteristic length (in this case, it corresponds to the projected height of the plate and depends on the angle of attack). From -10° to 10°, the Strouhal number is between 0.18 and 0.24, these values are consistent with vortex shedding on the wake of the profile.
Characteristic frequencies disappear at the angle of attack of 10.5° as expected. Indeed, the flow transition to super-critical regime occurs reducing the wake width and oscillations as explained before. Further, for higher AoA, frequencies related to an increasing wake width re-appear. It is consistent with results from the detachment point location seen earlier.
Power spectrum density is an additional tool to link dynamic features of the flow to lift coefficient time series variations, as vortex shedding by investigating the Strouhal number.

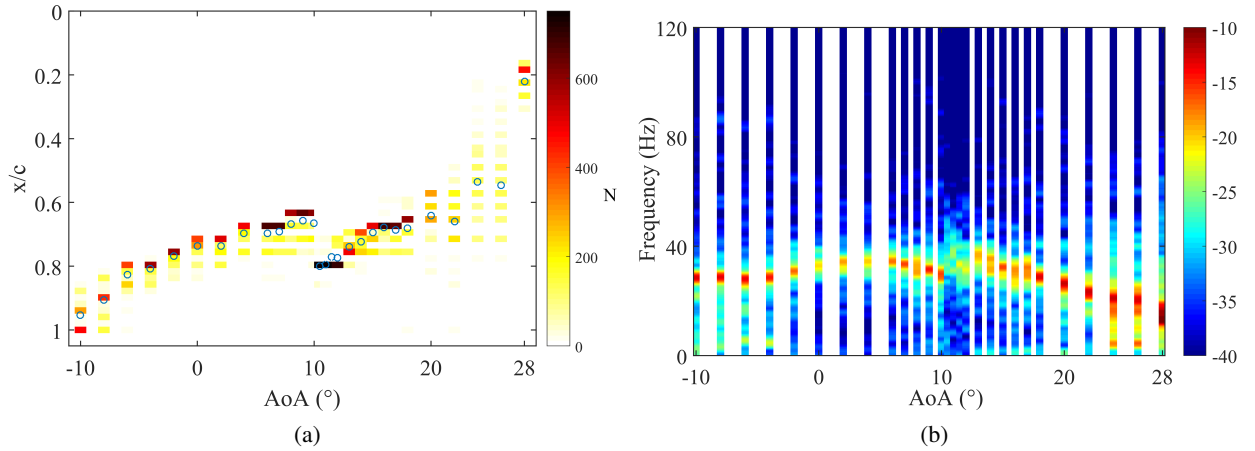

Figure 6: (a) Detachment point location ; (b) Lift coefficient spectrum for increasing AoA

This dynamic investigation based on time-resolved PIV and forces time-series motivated further work to undertake the analysis of vortex shedding in the wake. The next section will confirm these observations, revealing vortices helped by the vortex detection method.

3.4 Vortex boundary identification

The vortex identification algorithm using the 2 criteria is able to characterize the boundary of vortices, only considering the topology of the velocity field. The principal purpose of implementing this method is to identify the flow topology around this plate to link the flow topology to lift variation. Two wide fields have been treated to validate the usefulness of the 2 criteria and hypothesis concerning transition to turbulence.
To follow our purpose, boundaries corresponding to $|\Gamma_2| = \frac{2}{\pi} \approx 0.64$ are drawn in figure 7. These isocurves show the limit between convection and rotation, the part inside the boundary corresponds to the rotating area. Figure 7(a) represents a wide field at 10° with N = 48. It clearly reveals the vortices position in the wake, we observe large asymmetric contra-rotating vortices typical to Von Karman vortex street. Figure 7(b) shows the wide field at 10.5°, just after the transition. In this case, the wake is reduced as vortices and the most interesting part is the topology difference, here we have symmetric contra-rotating vortices. This two-bubble symmetric flow is a consequence of the transition to the super-critical regime and it explains

the important decrease of fluctuations on lift-coefficient time series Rodríguez et al. (2015) compares to two-bubble asymmetric flow.

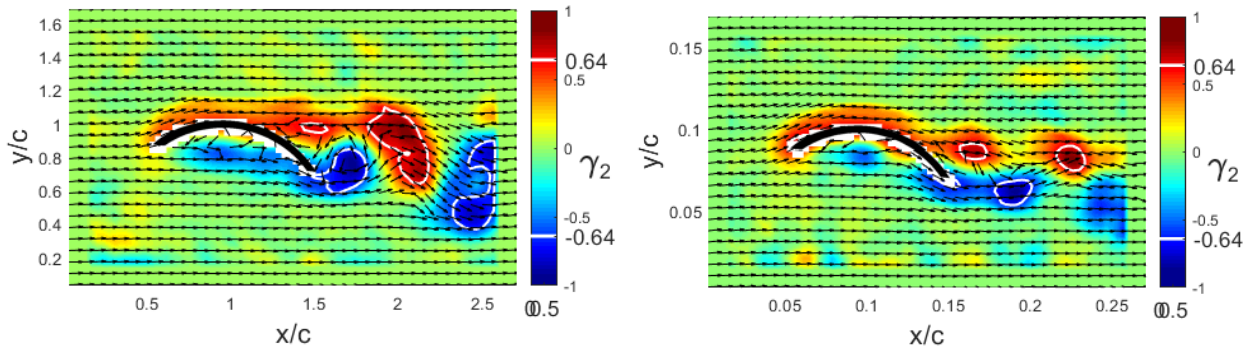

Figure 7: Vortex boundary computation for $|\Gamma_2| = \frac{2}{\pi}$ at $Re = 1.82.10^5$ (a) Sub-critical regime AoA = 10°; (b) Super-critical regime AoA = 10.5°

This method is a powerful tool to identify vortices and the topology of the flow around this plate. It confirms our expectations on the transition from sub-critical to super-critical state observed in previous parts of the study. For further work, a computation of the lift from velocity circulation on vortex contour may highlight vortices influence on lift variations and in general on the high camber plate behaviors.

4 Conclusion

In this study, we developed and improved several post-processing tools to investigate velocity fields from time-resolved PIV on a high-camber 2D section. The lift coefficient computation from velocity circulation compares reasonably well to the lift coefficient obtained from the hydrodynamic balance. Moreover, variations and knee-points of both curves presented are simultaneous. This statement enables a dynamic investigation based on sectional lift coefficient time series and the corresponding velocity fields focused on the lift jump observed at 10° AoA. It reveals a correlation between flow features as the wake width and oscillation amplitudes shown on velocity fields and the value and variations of the sectional lift coefficient. The discontinuity detected on the spectral density analysis representing vortex shedding frequencies and on the separation point location confirmed the hypothesis of a transition to turbulence. The vortex boundary identification method supports the hypothesis revealing a reorganization of the flow topology in the wake of the high-camber plate. The topology of the wake switches from a two-bubble asymmetric flow to two-bubble symmetric flow characteristic to a transition from a sub-critical to a super-critical regime.
Future work will implement a computation of the lift from velocity circulation on vortex contours. This study should not only focus on the wake but also on the leading edge vortex. The leading edge vortex has a significant contribution to the lift. This may highlight vortices influence on the high camber plate behaviors and lift variations in general.

References

Bot P, Rabaud M, Thomas G, Lombardi A, and Lebret C (2016) Sharp transition in the lift force of a fluid flowing past nonsymmetrical obstacles: Evidence for a lift crisis in the drag crisis regime. *Physical review letters* 117:234501

Dantec (2013) *DynamicStudio Users Manual*

Graftieaux L, Michard M, and Grosjean N (2001) Combining piv, pod and vortex identification algorithms for the study of unsteady turbulent swirling flows. *Measurement Science and technology* 12:1422

Habert B (2018) Etude dynamique d'un profil mince fortement cambr. internship report, IRENav Brest, France

Hein BR and Chopra I (2007) Hover performance of a micro air vehicle: Rotors at low reynolds number. *Journal of the American Helicopter Society* 52:254–262

Laitone E (1996) Aerodynamic lift at reynolds numbers below 7 x 10 exp 4. *AIAA journal* 34:1941–1942

Lombardi A (2014) *Experimental Analysis of a Highly Cambered Thin Profile*. Ph.D. thesis. MSc Thesis, University of Strathclyde

Marchand JB (2014) *Experimental Analysis and Numerical Simulation of Foil Sections for Tidal Turbine Application*. Ph.D. thesis. Paris, ENSAM

Rodríguez I, Lehmkuhl O, Chiva J, Borrell R, and Oliva A (2015) On the flow past a circular cylinder from critical to super-critical reynolds numbers: Wake topology and vortex shedding. *International Journal of Heat and Fluid Flow* 55:91–103

Sunada S, Yasuda T, Yasuda K, and Kawachi K (2002) Comparison of wing characteristics at an ultralow reynolds number. *Journal of aircraft* 39:331–338

Welch P (1967) The use of fast fourier transform for the estimation of power spectra: a method based on time averaging over short, modified periodograms. *IEEE Transactions on audio and electroacoustics* 15:70–73